Materials Science and Engineering A 550 (2012) 243–253

Contents lists available at SciVerse ScienceDirect

Materials Science and Engineering A

journal homepage: www.elsevier.com/locate/msea

Subsurface characterization of an oxidation-induced phase transformation and twinning in nickel-based superalloy exposed to oxy-combustion environments☆

Jingxi Zhu[a,b,*], Gordon R. Holcomb[c], Paul D. Jablonski[c], Adam Wise[b], Jia Li[b], David E. Laughlin[b], Seetharaman Sridhar[a,b]

[a] National Energy Technology Laboratory, Pittsburgh, PA 15236, USA
[b] Department of Materials Sciences and Engineering, Carnegie Mellon University, Pittsburgh, PA 15213, USA
[c] National Energy Technology Laboratory, Albany, OR 97321-2198, USA

ARTICLE INFO

Article history:
Received 20 March 2012
Accepted 20 April 2012
Available online 28 April 2012

Keywords:
Oxy-fuel combustion
High temperature oxidation
Phase transformation
Superalloy

ABSTRACT

In the integration of oxy-fuel combustion to turbine power generation system, turbine alloys are exposed to high temperature and an atmosphere comprised of steam, CO_2 and O_2. While surface and internal oxidation of the alloy takes place, the microstructure in the subsurface region also changes due to oxidation. In this study, bare metal coupons of Ni-base superalloys were exposed in oxy-fuel combustion environment for up to 1000 h and the oxidation-related microstructures were examined. Phase transformation occurred in the subsurface region in Ni-based superalloy and led to twinning. The transformation product phases were analyzed through thermodynamic equilibrium calculations and various electron microscopy techniques, including scanning electron microscopy (SEM), orientation imaging microscopy (OIM) and transmission electron microscopy (TEM). The mechanism by which the phase transformation and the formation of the microstructure occurred was also discussed. The possible effects of the product phases on the performance of the alloy in service were discussed.

1. Introduction

In oxy-fuel combustion, hydrocarbon fuel is burnt with oxygen instead of air and consequently the need to separate CO_2 from the other off gases such as N_2 is eliminated. This allows for a more efficient and cost-effective CO_2 capture, and has the potential capability of supplying CO_2 for sequestration or enhanced oil recovery (EOR) [1,2].

Promising integrated oxy-fuel combustion and turbine power generation systems are being developed, for example, the Basic S-Graz Cycle [2] and the Clean Energy Systems Oxy-fuel Cycle [3]. The working fluid for the former is ~77% H_2O, 23% CO_2, and 0.5% O_2, and the latter is ~90% H_2O, 10%CO_2 and 0.2% O_2. These environments have high carbon and oxygen activities that are different from the air-fired fuel turbine environment. Conventional steam turbines can be used as high pressure turbines (HPT) and low pressure turbines (LPT), but it is the intermediate pressure turbines (IPT) that experience the highest temperatures. Further development of the oxy-combustion technology will push the temperature even higher [3]. Therefore, for the next generation of higher efficiency power plants, higher temperature capability is required for oxy-fuel fired gas turbine materials than the current generation of turbines.

Research efforts have been focused on maintaining the mechanical integrity of the alloy in service by effectively controlling the microstructures that can compromise such integrity, such as the alloy grain boundaries, the secondary phases precipitated at grain boundaries, including various carbides and embrittling topological close-packed (TCP) phases, and the interface between these secondary phases and the alloy matrix [4–6]. Focus has also been on the long-term stabilization of fine strengthening precipitates that improve the creep strength of the alloy at the use temperature [7]. Moreover, the high carbon and oxygen activity in the atmosphere may lead to a different oxidation behavior that affects the

☆ *Disclaimer*: This report was prepared as an account of work sponsored by an agency of the United States Government. Neither the United States Government nor any agency thereof, nor any of their employees, makes any warranty, express or implied, or assumes any legal liability or responsibility for the accuracy, completeness, or usefulness of any information, apparatus, product, or process disclosed, or represents that its use would not infringe privately owned rights. Reference herein to any specific commercial product, process, or service by trade name, trademark, manufacturer, or otherwise does not necessarily constitute or imply its endorsement, recommendation, or favoring by the United States Government or any agency thereof. The views and opinions of authors expressed herein do not necessarily state or reflect those of the United States Government or any agency thereof.

* Corresponding author at: Carnegie Mellon University, Dept. Materials Science and Engineering, Pittsburgh, PA 15213, USA. Fax: +1 412 268 7596.
E-mail addresses: jingxiz@andrew.cmu.edu (J. Zhu), holcombg.alb.or@netl.doe.gov (G.R. Holcomb), Paul.Jablonski@NETL.DOE.GOV (P.D. Jablonski), adamwise@andrew.cmu.edu (A. Wise), jiali@andrew.cmu.edu (J. Li), dl0p@andrew.cmu.edu (D.E. Laughlin), sridhars@andrew.cmu.edu (S. Sridhar).

0921-5093/$ – see front matter © 2012 Elsevier B.V. All rights reserved.
http://dx.doi.org/10.1016/j.msea.2012.04.066

Table 1
The nominal composition of the In 939 alloy, in weight percent.

Ni	Co	Cr	Al	Ti	Ta + Nb	W	C
48.36	18.9	22.5	1.9	3.8	2.4	2	0.14

mechanical properties of the turbine [8]. These research activities may help extend the usable critical temperature of nickel superalloys.

Materials performance of Ni-base superalloys and alloy/coating systems has been evaluated in the oxy-fuel turbine environments to understand the oxidation products and their microstructure [6]. The oxidation rate of Ni-base superalloys is low and with protective parabolic behavior at 1021 K and below, but the rate increases significantly at 1094 K, although remaining parabolic. In terms of effective metal loss, internal oxidation was the primary factor for the Ni-base alloys [6].

As shown in Ref. [6], both bare and coated alloys are present in a Siemens SGT-900 gas turbine proposed for the second-generation design of the Clean Energy Systems Oxy-fuel Cycle. The oxidation of the bare alloy is important because the un-coated backside of the blades is cooled with the same atmosphere as the coated front side, albeit at a lower temperature. Bare alloy oxidation is also important should the coating fail.

This work examined the microstructure of several bare Ni-based superalloys (Inconel 738, Inconel 939 and Udimet 520) oxidized under a range of oxy-fuel conditions. As will be shown, a sub-surface phase was seen to precipitate in nearly all cases and to analyze this further, the present study focuses on the γ′ precipitate strengthened Inconel® 939 Ni-based superalloy oxidized under steam-CO_2–O_2 atmospheres, and aims to:

(i) characterize the surface and sub-surface oxidation structure;
(ii) investigate the oxidation-related phase transformation of the strengthening γ′ precipitates;
(iii) identify the phase transformation products;
(iv) understand the mechanism of such transformation; and
(v) assess the effects of the transformation or products on the integrity of the alloy in use.

2. Experimental

Oxidation coupons of bare alloys were isothermally exposed at high temperatures in a tube furnace for various durations with a flowing atmosphere of steam and various percentage of CO_2, O_2 and H_2. The flow rate was 25 cm/min at temperature. The oxidation coupons were exposed for up to 1000 h. Inconel® 939 was used in the present work as a case study. The alloy underwent solutioning and aging heat treatments and resulted in a γ phase alloy with γ′ as strengthening precipitates. The nominal composition of this Ni-based alloy is shown in Table 1. The furnace heating and cooling rates were mild, on the order of 100–200 K per hour.

After oxidation exposure, the metallographically polished cross-sections of the alloy coupons were examined with scanning electron microscopy (SEM), energy dispersive X-ray spectroscopy (EDS) and orientation imaging microscopy (OIM).

In the thickness direction of the alloy coupon, the oxidation products consisted of (i) external scale, (ii) internal oxidation zone, and (iii) a twinning zone in which twins were prevalent and contained a hitherto un-identified phase, referred to as the "U phase". The reaction products are schematically shown in Fig. 1. The focus of the current study is to characterize the phases that constitute these regions, and the twinning zone is particularly interesting.

Hence, two thin foil specimens were prepared by in situ liftout technique with a FEI Nova 600 DualBeam system. The location

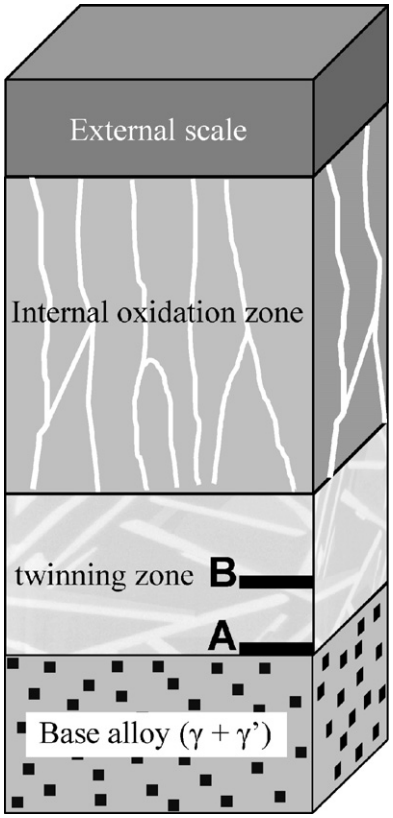

Fig. 1. Schematic cross section of the oxidized sample with the key microstructural features and the location where the two liftout specimens were sampled.

where these two specimens were sampled is schematically shown in Fig. 1: specimen A was taken at twinning zone/base alloy boundary and specimen B was sampled at approximately half depth of the twinning zone. The two specimens were fine polished with focused ion beam (FIB) and examined with SEM, EDS and electron backscatter diffraction (EBSD). Then, specimen B was further thinned to an electron transparent foil and studied with an FEI Tecnai F20 transmission electron microscope (TEM), utilizing techniques including electron diffraction and scanning transmission electron microscopy (STEM) coupled with EDS.

3. Results and discussion

3.1. The overall oxidation structure and the interesting features

Fig. 2 shows the cross-section of the overall oxidation structure of the study alloy, after 1000 h of isothermal oxidation at 1094 K, in an atmosphere of steam with 10% CO_2 and 0.2% O_2. An external scale made up mainly of Cr_2O_3 formed on the alloy surface, with an average thickness of 5.3 μm. Beneath the external scale was an internally oxidized region, with an average depth of 15 μm. The dark substances seen in this region were thread-like internal oxides embedded within the un-oxidized alloy, which were commonly observed for superalloys strengthened with γ′ [prototype: $Ni_3(AlTi)$] precipitates [9]. In the case of In 939, these internal oxides were typically Al_2O_3, sometimes TiO_x, and $NiAl_2O_4$ as well under certain oxidation conditions [10]. It has been well known that grain boundaries of the alloy provide fast diffusion paths for oxygen inward diffusion; hence, the internal oxides display a thread-like morphology [10]. Underneath the internal oxidation zone, it was the twinning zone, in which a large number of grains appeared to be twins of one another, as highlighted by the rectangle in Fig. 2. More interestingly, a few internal oxide threads, as indicated by

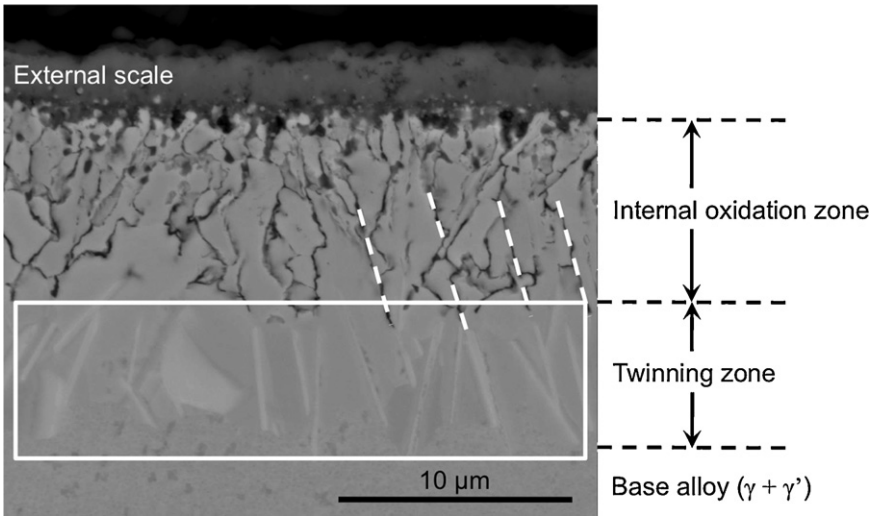

Fig. 2. Secondary electron (SE) image of overall oxidation structure of In 939 alloy after 1000 h of isothermal oxidation at 1094 K, in an atmosphere of steam with 10% CO_2 and 0.2% O_2.

the dotted lines in Fig. 2, seemed to grow in a certain direction into the twinning zone such that they were almost parallel to each other. Moreover, in the twinning zone, the ends of these oxides threads connected to slab-shaped grains that extended toward the base alloy in the same direction as the threads. This strongly indicated that a relation must exist between the internal oxides and the slab-shaped grains.

A brief survey of the alloy grain orientation and grain boundary characteristics in the internal oxidation zone and twinning zone was performed through EBSD, with a relatively large step size. The sample drift incurred during acquiring was corrected manually. Fig. 3a is the secondary electron micrograph of the area whose orientation is analyzed with respect to face-centered-cubic (FCC) Ni, and the corresponding orientation map is shown in Fig. 3b. This inverse pole figure (IPF) map was cleaned with "grain dilation" and "average orientation" procedures with TSL OIM analysis v5.0 software. First, it appeared that the growth mode of the internal oxide threads was intergranular growth; second, a number of $\Sigma 3$ grain boundaries were present in both internal oxidation zone and twinning zone, and these grain boundaries were, in fact, mostly twin boundaries; third, a few slab-shaped grains, indicated by the arrows labeled "A", could not be recognized as Ni and appeared in black color in the orientation map, meaning "no solution in indexing". Therefore, the crystallographic space group of these high aspect-ration grains was not of FCC Bravais lattice, and hence they were a different phase. The phase constituting these grains will be referred to as "U" phase from hereon. To examine the U phase grains in relation to the surrounding alloy grains (will be referred as Ni-matrix grains from hereon) on a finer resolution, a thin-foil specimen was lifted out from the location indicated in Fig. 3b, which was near the boundary of the twinning zone and the base-alloy. One should note that a cross-sectional liftout procedure performed on a metallographically prepared cross-section makes the thin-foil plane view relative to alloy surface.

In the secondary electron micrograph of the liftout foil, Fig. 4a, $\gamma + \gamma'$ base alloy grains are clearly visible. Fig. 4b shows the orientation map of the rectangle area on the foil, with a pixel resolution of 50 nm. This IPF map was processed with the same procedure as Fig. 3b. When pixels with index confidence levels below 0.2 were discarded, the U phase grains were revealed in the IPF map, labeled "U". Furthermore, upon examining the orientation of each indexed grain, which were expressed in sets of three Euler angles in Fig. 4b, a rather peculiar configuration of the U phase grains, Ni-matrix grains, and $\Sigma 3$ boundaries was found.

In Fig. 4b, the Ni-matrix grains marked with "A" are, in fact, all orientated in the same direction; and grains that are labeled as "B" are twins of the "A" grains. The U phase grain slab that lies among the "A" grains is parallel to the twin boundaries dividing the "A" and "B" grains. Another example of such configuration can be seen with a pair of twin grains labeled as "C" and "D", beside which is a U phase grain parallel to their twin boundary. This configuration implied that the $\{1\,1\,1\}$ planes of FCC Ni-matrix were the coherent planes between the two phases.

It should also be noticed that one may not find one or more pairs of twins and twin boundaries parallel to every U phase grain. This was probably because of constraints posed by the surrounding Ni-matrix grains during the nucleation and growth of U phase grains, such that the aforementioned configuration was incomplete for some cases.

Knowing the presence of the U phase, it would be of both practical and scientific interest to understand how and why it formed and what crystallographic structure it had.

3.2. *The formation of the U phase*

To address the first question, it is necessary to determine whether the formation of U phase is related to high temperature oxidation and how general its presence is in these alloys. Table 2 summarizes the observations made on In 939 alloy oxidized under various conditions, including temperature, oxidation duration, atmosphere and the surface condition of the oxidation coupons. More oxidation results under these conditions can be found in reference [6]. The bare alloy samples all had visible twinning and U phase regions, except that one sample oxidized at 903 K was ambiguous, probably because the depth of the oxidation structure was small at this temperature. The samples with thermal barrier coating showed no twinning or internal oxidation. The U phase grains were also absent in the thermal barrier coated samples. It appeared, therefore, that when internal oxidation occurred, twinning and U phase were present simultaneously, regardless of the depth of internal oxidation.

Furthermore, with a brief OIM survey of the bulk alloy away from the oxidized surface, as displayed in Fig. 5, isothermal holding of the alloy at high temperature resulted in coarsening of both alloy grains and carbides. Other than that, the alloy bulk remained in the $\gamma + \gamma'$ phases after oxidation. Substantial twinning was not observed anywhere in the bulk alloy grains. It was hence evident from the results shown in Table 2 and Fig. 5 that the formation of

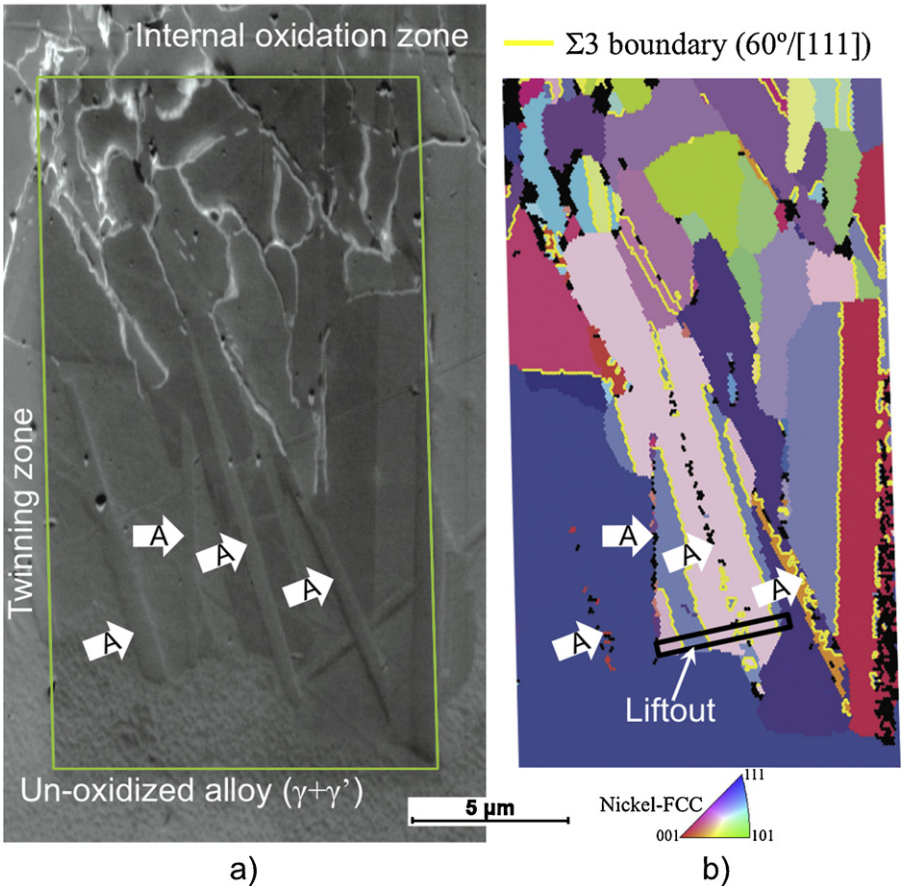

Fig. 3. (a) SE image of the cross-section of internal oxidation zone and (b) the corresponding inverse pole figure (IPF) orientation map of the area as indicated in (a). The color legend of the orientation map is shown below the IPF map.

the twinning zone was related to the oxidation of the alloy, particularly the internal oxidation, which was in support of the previous statement.

If one considers the following change in the phase constituents to be the phase transformation:

$$(\gamma + \gamma') \rightarrow \text{Ni-matrix (FCC)} + \text{U phase}, \quad (1)$$

the driving force would likely be either temperature change or chemical composition change, assuming equilibrium. In this study, oxidation was isothermal; therefore the change in chemical composition, if any, would be a probable cause for such phase transformation.

This would also make sense, since the twinning zone always located beneath the internal oxidation zone; and results in the previous section revealed that there was a correlation between internal oxidation and U phase grains.

For this reason, chemical compositions on the two sides of equation 1 were obtained, and Thermo-Calc was used to predict

Table 2
U phase presence in In 939 alloy oxidized under various conditions.

	Temperature (K)	Duration (h)	Atmosphere: steam (balance) +			Internal oxidation visible?	Twinning and U Phase visible?
			CO_2 (%)	O_2 (%)	H_2 (%)		
Bare alloy	903	500	10	0.2	0	Yes	Yes
	903	1000	10	0.2	0	Yes	Ambiguous
	966	1000	10	0.2	0	Yes	Yes
	1021	500	10	0.2	0	Yes	Yes
	1021	1000	10	0.2	0	Yes	Yes
	1023	1000	10	0.2	0	Yes	Yes
	1023	1000	10	0	0.14	Yes	Yes
	1094	250	10	0.2	0	Yes	Yes
	1094	500	10	0.2	0	Yes	Yes
	1094	1000	10	0.2	0	Yes	Yes
	1094	1000	30	0.2	0	Yes	Yes
	1094	1000	50	0.2	0	Yes	Yes
	1094	336	0	100	0	Yes	Yes
With thermal barrier coating	903	1000	10	0.2	0	No	No
	1021	1000	10	0.2	0	No	No
	1094	1000	10	0.2	0	No	No

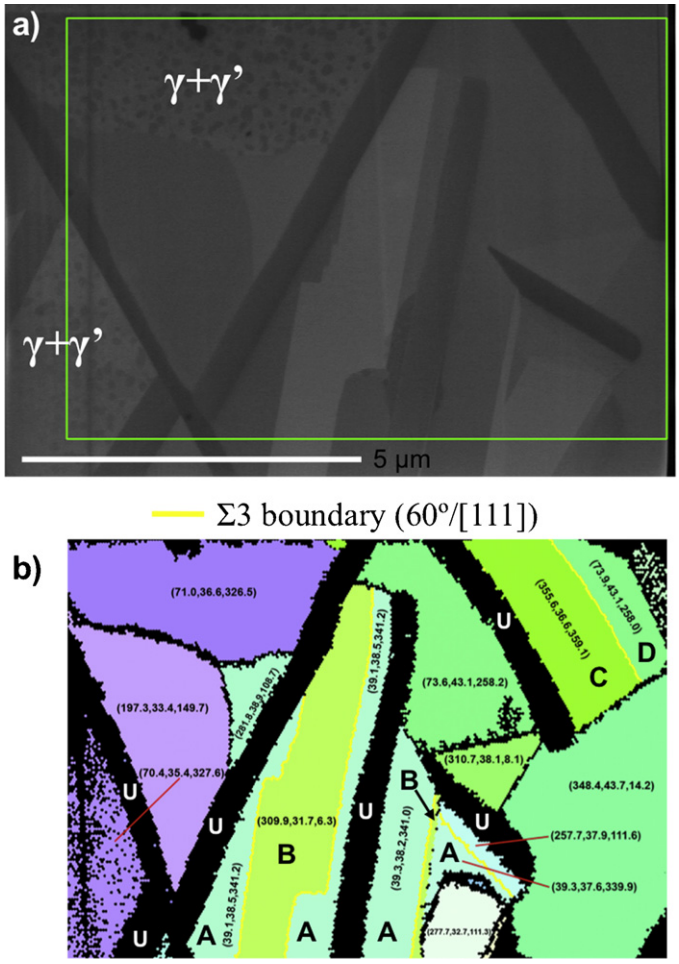

Fig. 4. (a) SE image of the liftout specimen and (b) the corresponding IPF orientation map of the area as indicated by the rectangle in (a).

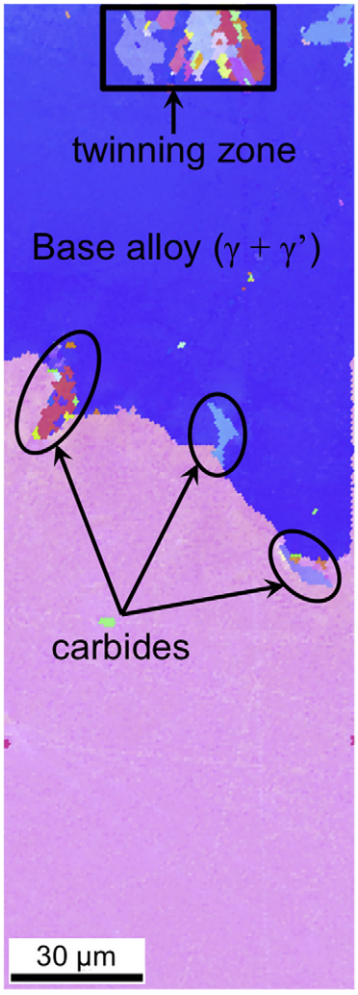

Fig. 5. IPF orientation map of a large area on the oxidation cross-section.

equilibrium phases. The chemical composition of the $\gamma+\gamma'$ phases was taken as the nominal alloy composition, and the twinning zone composition was obtained by weighting the EDS analysis on the Ni-matrix grains and U phase grains by their relative aerial fraction in the micrograph, assuming the two phases had similar densities.

Fig. 6 shows the EDS results in the twinning zone. EDS spectra were taken in both Ni-matrix grains and U phase grains, which were indicated in the micrograph with black and white stars, respectively. The average compositions of the two types of locations are shown as well. The standard deviation was small when averaging the two compositions. It was seen that the contents of the three major alloying elements: Ni, Co and Cr of the Ni-matrix grains were close to those of the nominal composition of the alloy while the Al and Ti contents were much lower. As for the U phase composition, Ti content was noticeably higher; Al and Ni contents were slightly higher and Cr and Co contents were much lower than those of the nominal composition. Also, a quite high Ta content in the U phase grain was observed.

The overall composition of the twinning zone was then estimated from these EDS results. The aerial fractions of the U phase grains and Ni-matrix grains were determined using ImageJ, resulting in Ni-matrix % = 75.56% and U phase % = 24.44%. The compositions of Ni-matrix and U phase were then weighted by these percentages to obtain an overall composition of the twinning zone, which is shown in Table 3.

Next, the equilibrium phases for the nominal alloy composition and weighted twinning zone compositions were determined with Thermo-Calc ver. S [11] using the Ni-Data v.8 [12] database. All the phases in this database were included in the calculation. The results are listed in Tables 4 and 5.

Table 3
Overall composition of the twinning zone, obtained by weighting the compositions of Ni-matrix grains and U phase grains by their aerial fractions.

wt%	Al	Ti	Cr	Co	Ni	Nb	Ta	W
Weighted composition	0.66	2.42	19.32	18.93	52.92	1.03	2.19	2.51

For the nominal alloy composition, Thermo-Calc predicted three phases: solid solution FCC phase, precipitation-strengthening γ' (prototype: Ni_3Al, $L1_2$ structure) phase and a minor amount of σ phase. The σ phase is irrelevant to the U phase in the twinning zone, because it has over 50 wt% of Cr, whereas the phase of interest, i.e. U phase, has a quite low Cr content. The weighted twinning zone composition resulted in two phases: FCC and η phase. The FCC

Table 4
Equilibrium phase compositions obtained with Thermo-Calc [11] using the Ni-Data database [12] for nominal alloy composition and weighted twinning zone composition.

Nominal alloy composition		Weighted twinning zone composition	
Equilibrium phase	wt%	Equilibrium phase	wt%
FCC	56.46	FCC	83.79
γ'	36.70	η	16.21
σ	6.84		

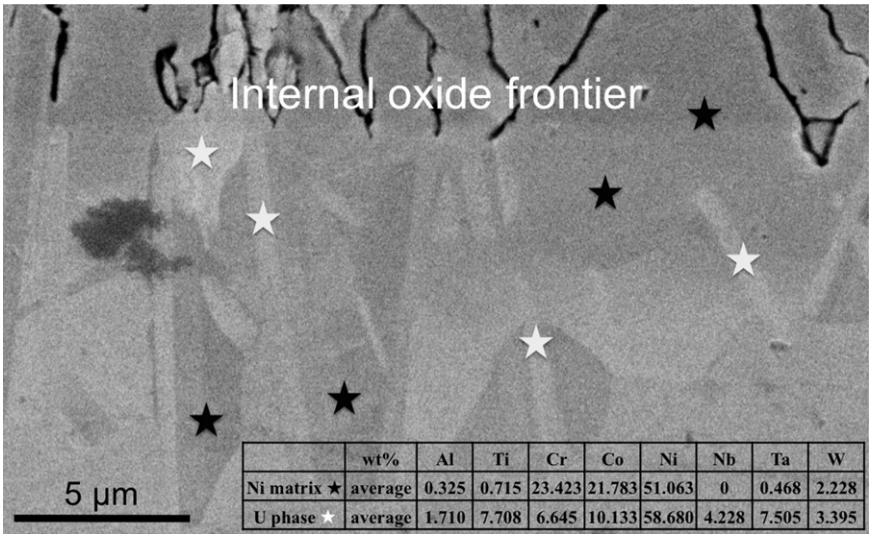

Fig. 6. Cross-section SE image and the average chemical composition of the two types of locations.

Table 5
The elemental compositions of the equilibrium phases obtained via Thermo-Calc [11] using the Ni-Data database [12] for nominal alloy composition and Weighted twinning zone composition.

wt%	Nominal alloy composition			Weighted composition	
	FCC	γ′	σ	FCC	η
Ni	40.25	67.77	13.19	50.89	63.50
Ti	0.31	9.88	0	0.57	11.98
Ta	0.21	4.58	0	1.04	8.12
Co	24.43	9.02	26.29	20.74	9.56
Nb	0.04	1.58	0	0.27	4.97
Cr	31.68	1.74	58.13	23.00	0.29
Al	0.44	4.50	0.01	0.49	1.58
W	2.65	0.93	2.39	3.00	0

phase is also a solid solution, but has higher Ni and lower Co and Cr contents compared to those of the nominal alloy composition, which can be seen in Table 5. The prototype for η phase is Ni_3Ti ($D0_{24}$).

Therefore, based on EDS analysis and in the Thermo-Calc analysis, the phase transformation: $(\gamma+\gamma') \rightarrow FCC+\eta$, is favored by thermodynamic equilibrium; and this is driven by a chemical composition change from nominal to the twinning zone composition, most probably because of internal oxidation. This also indicated that U phase was likely the η phase. If so, Thermo-Calc should predict η phase for U phase composition, and this would help identify the U phase.

Therefore, the same Thermo-Calc equilibrium phase calculation was carried out for Ni-matrix and U phase compositions to test the previous Thermo-Calc outcomes and the results are shown in Tables 6 and 7.

The Ni-matrix composition resulted in a single solid solution FCC phase whose composition was quite close to that of the twinning zone FCC phase (Table 5). This was consistent with the EBSD results. However, a total of four phases were predicted for the U phase composition by Thermo-Calc. Besides the expected η phase, FCC and γ′ phases were also predicted, along with a very small fraction of μ phase. μ-phase belongs to the category of topologically close packed (TCP) phases, which is usually detrimental.

The different phase constituents given by Thermo-Calc for the U phase composition and weighted twinning zone composition should be attributed the solubility of individual elements in FCC, γ′, η and μ phases. The reason why γ′ and μ were present in the calculation results for U phase composition was probably that the Ti and Ta contents exceeded their solubility in FCC and η phase, and resulted in the γ′ phase and similarly, excess W resulted in μ phase.

In addition to EDS spot analysis, elemental mapping was also carried out on the two thin foil specimens lifted out from the twinning zone/base alloy boundary and 1/2 depth of the twinning zone. The elemental maps in Fig. 7 showed that for both specimens, Ti was mostly enriched in U phase grains, while the U phase grains were also quite depleted of Cr and Co with respect to surrounding grains. Enrichment of Ni was more visible in the specimen from the 1/2 depth of the twinning zone, as well as for the refractory elements, such as Nb, Ta and W. This should be the reason why the U phase grains always appeared brighter in backscattered electron micrographs.

The enrichment of Ni and Ti in the U phase grains shown by elemental mapping supports the Thermo-Calc result that the U phase being Ni_3Ti. Also, although the slab-shaped U phase grains had

Table 6
Equilibrium phase compositions obtained with Thermo-Calc [11] using the Ni-Data database [12] for Ni-matrix and U phase compositions.

Ni-matrix composition		U phase composition	
Equilibrium phase	wt%	Equilibrium phase	wt%
FCC	100	η	63.78
		FCC	22.66
		γ′	11.91
		μ	1.66

Table 7
The elemental compositions of the equilibrium phases obtained via Thermo-Calc [11] using the Ni-Data database [11] for Ni-matrix and U phase compositions.

wt%	Ni-matrix composition	U phase composition			
	FCC	η	FCC	γ′	μ
Ni	51.10	63.51	44.83	67.00	9.69
Ti	0.70	10.71	0.32	6.68	0
Ta	0.50	9.90	0.83	8.33	0.45
Co	21.80	8.32	17.39	5.53	12.06
Nb	0	5.65	0.30	4.42	0.09
Cr	23.40	0.19	26.87	1.45	13.42
Al	0.30	1.73	0.40	4.25	0
W	2.20	0	9.08	2.35	64.29

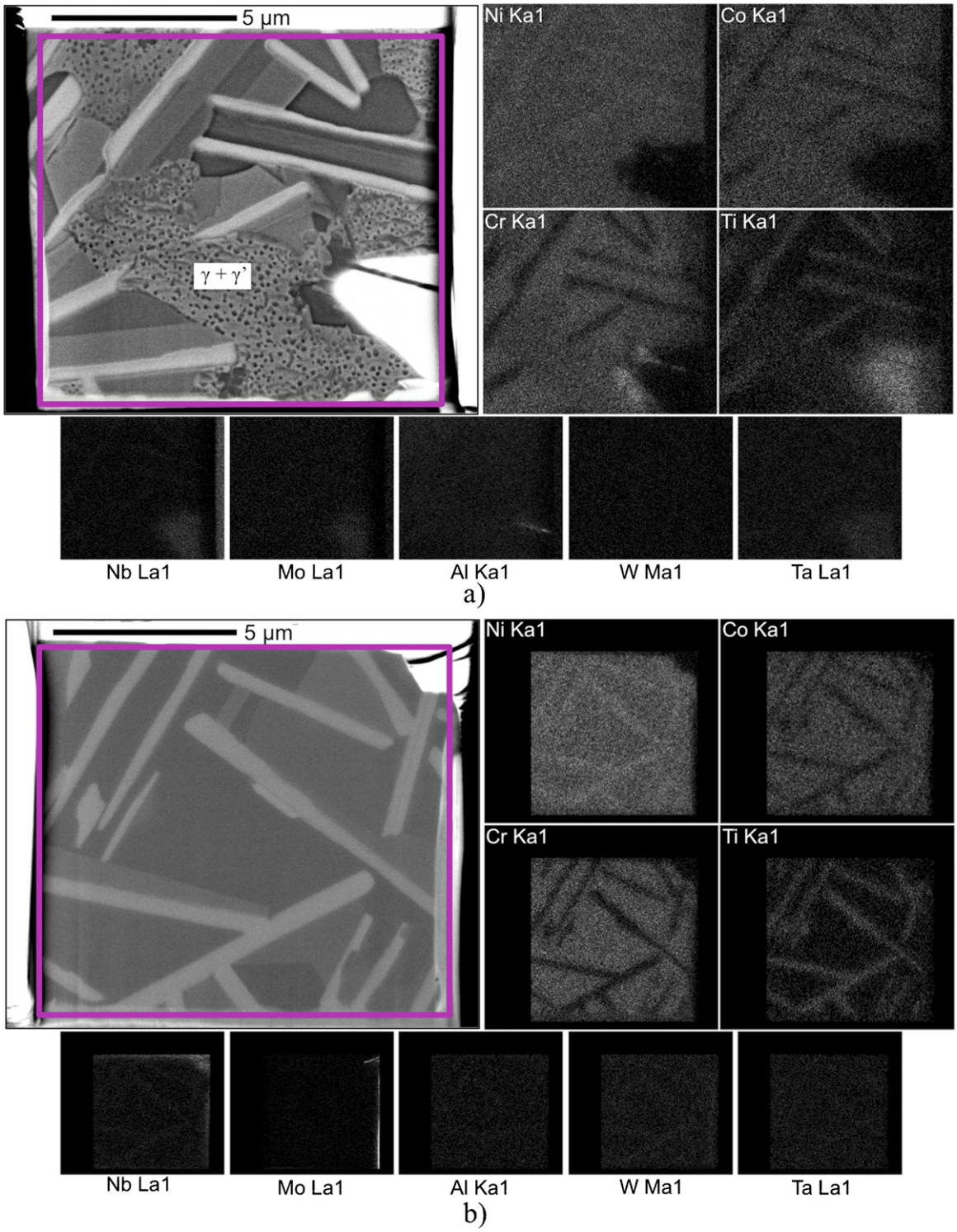

Fig. 7. Plane view BSE image of specimens lifted out from (a) twinning zone/base alloy boundary and (b) 1/2 depth of the twinning zone; and corresponding EDS maps of the major alloying elements.

some resemblance to the characteristics of TCP phases [13], μ phase was temporarily ruled out for the fact that in the calculation result, μ phase did not contain any Ti, but the elemental mapping clearly showed otherwise. Also, the precipitation of μ phase might require either a longer exposure time than 1000 h or a temperature higher than 1094 K [13]. Nevertheless, μ phase will be revisited later as a TCP phase in comparison of the possible detrimental effects of the U phase on the alloy performance.

Besides the chemical composition change being the driving force for many phase transformations, stress and/or strain often also contribute to such transformation and strongly influence the nature and morphology of the product phase [14]. Sometimes in the absence of a chemical driving force, stress alone can cause phase transformation to occur, which is known as stress induced phase transformation [15,16]. When EBSD was performed on the above-mentioned two liftout specimens, indicator of strain was found on

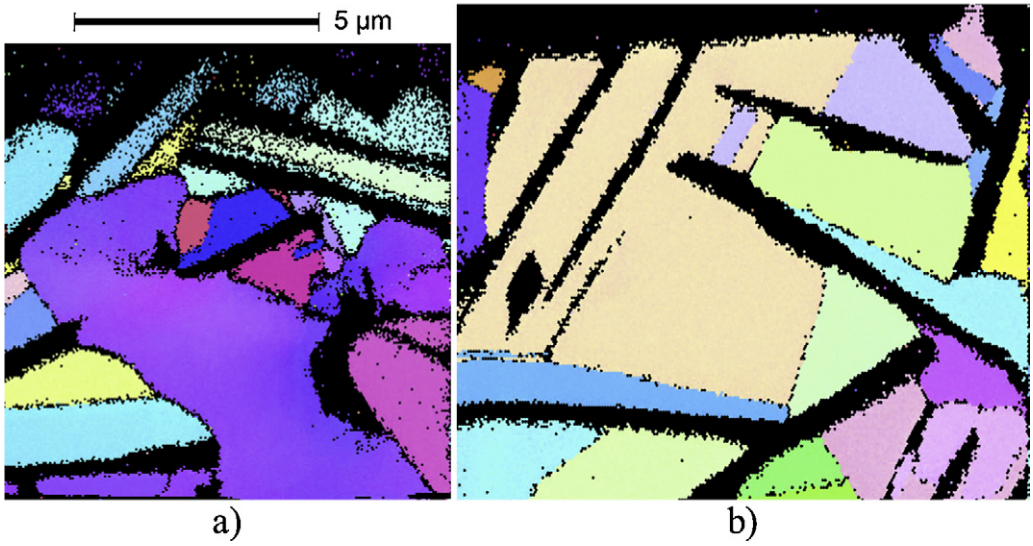

Fig. 8. IPF orientation map of (a) specimen A (at twinning-zone/$\gamma+\gamma'$ boundary) and (b) specimen B (at 1/2 depth of twinning zone). The scale bar applies for both maps.

the specimens that was lifted out from the twinning-zone/base-alloy boundary. The indicator of strain is usually a color gradient in the IPF orientation map, also known as the strain-induced lattice rotation [17]. In this case, such lattice rotation is normally very small between the neighboring pixels in the map, resulting in a misorientation that is below the threshold to define a grain boundary.

The two IPF orientation maps shown in Fig. 8 were obtained with the same collection parameters, such as acceleration voltage = 25 kV, beam current = 9.5 nA, step-size = 50 nm; and went through same post-collection processing procedures: grain dilation and removal of pixels with indexing confidence lower than 0.2. If one compares these two maps, it is easy to find strained areas on the specimen lifted out from the twinning-zone/$\gamma+\gamma'$ boundary, whereas the specimen lifted out from the 1/2 depth of the twinning zone, where the microstructure has fully developed and may be locally stabilized, is relatively strain free. This indicated that in the process of transforming from $\gamma+\gamma'$ microstructure to the one present in the twinning zone, local stress might have been a contributing factor.

The specimen in Fig. 8a is of interest for the following reasons: first, there is a large $\gamma+\gamma'$ grain that is strained; second, there is a necking area in this grain that is associated with the growth of a U phase grain, as indicated on Fig. 9b. Two U phase slabs seem to be growing into each other along the directions of the arrows, separated by the $\gamma+\gamma'$ grain, and having formed a necking area in the $\gamma+\gamma'$ grain. Possibly, the U phase slabs might have already connected somewhere else, that they are consuming the $\gamma+\gamma'$ grain at the necking area. Finally, this particular necking area in the $\gamma+\gamma'$ grain is strained. To analyze if the strain in the necking area of the $\gamma+\gamma'$ grain is indeed associated with the growth of the U phase grain, the magnitude of the strain or the strain-induced lattice rotation must be quantified and the direction of the strain gradient must be determined as well.

Therefore, the raw OIM data was processed with a home-written program so that this $\gamma+\gamma'$ grain could be partitioned from the rest of the OIM data in Fig. 8a and an IPF map of the $\gamma+\gamma'$ grain could be generated by the TSL OIM analysis software, shown in Fig. 9a. Fig. 9b shows its location in the overall microstructure. An inverse pole figure was plotted for this grain, see Fig. 9c. It shows the projection of the normal direction of the sample reference frame onto the crystal reference frame (FCC). The average orientation of this grain is indicated by the symbol "✳" in Fig. 9c, which is close to the [1 1 2] direction of the crystal reference frame. The average orientation can be regarded as the orientation this grain would have assumed without strain. It can be seen in Fig. 9c that the orientation of this grain spreads about its average orientation, mostly along the (1 1 0) plane of FCC structure. Next, the misorientation of each pixel with

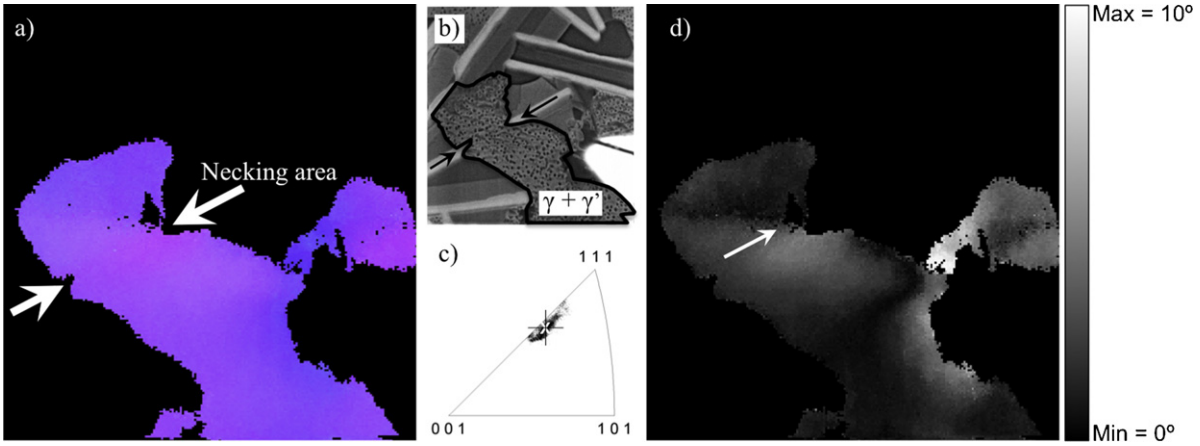

Fig. 9. (a) IPF map of a $\gamma+\gamma'$ grain at the twinning zone/base alloy interface that is strained; (b) BSE micrograph of the corresponding area of the IPF map; (c) inverse pole figure of normal direction (ND) of sample reference frame projected on the crystal reference frame; (d) misorientation map of the strained grain with respect to its average orientation, on a scale of 0–10°.

respect to the average orientation was calculated, and the resulting misorientation map is shown in Fig. 9d, on a scale of 0–10 degrees. It is evident from this map that the direction of the misorientation gradient (the arrow in Fig. 9d) is related to the U phase slab that the misorientation increases with decreasing distance to the U phase slab to the right of the $\gamma+\gamma'$ grain necking area. Therefore, it was probable that the growth of the U phase generated local strain to its surrounding grains.

Until this point, a likely chain of events that occurred during high temperature oxidation that leads to the formation of the twinning and U phase can be formulated as follows according to the depiction in Fig. 10.

As the internal oxidation progressed into the base alloy, Al and Ti in the close proximity were denuded from their original $\gamma+\gamma'$ configuration. Hence, the γ' phase in the base alloy was destabilized and dissolved (Fig. 10a), and the composition in this region probably changed into one that was close to the weighted twinning zone composition shown in Table 3. As predicted by Thermo-Calc in the equilibrium phase calculation, the phase transformation: $(\gamma+\gamma')\rightarrow$ FCC + η, is favored by thermodynamic equilibrium; and would be driven by a chemical composition change from nominal composition to that of the twinning zone composition because of internal oxidation. Also, it was shown that stress and strain was generated locally when γ' phase dissolved and the remaining elements partitioned into two phases, i.e. FCC and U phase (Fig. 10b). The stress and strain may be the reason why the U phase grains precipitate with a crystallographic relation to the Ni-FCC matrix, and twinning in the Ni-matrix grain may have occurred along with or after the precipitation of U phase slabs in order to relax the stress, which resulted in the formation of twinning zone with the peculiar configuration of the U phase grains, the Ni matrix grains and grain/phase boundaries (Fig. 10c). The question remains, however, whether the U phase is indeed the η phase in the thermodynamic prediction.

3.3. Identification of the U phase

To determine whether U phase is indeed the η phase or another phase, electron diffraction studies were carried out on the specimen lifted out from the 1/2 depth of the twinning zone.

Fig. 11b and c shows two zone axis diffraction (ZAD) patterns from a Ni-matrix grain and a U phase grain, respectively, along with the bright field image of these two grains (Fig. 11a). The zone axis of the Ni-matrix grain ZAD pattern is $[\bar{1}\,1\,\bar{2}]$. The ZAD pattern of the U phase grain has all the fundamental spots of the FCC-Ni structure, which are $(\bar{1}\,1\,1)$, $(1\,3\,1)$, $(2\,2\,0)$ and $(3\,1\,\bar{1})$, and super-lattice spots at half of the g_{hkl} vectors. However, if the U phase were indeed η phase (prototype Ni_3Ti, $D0_{24}$ structure), the super-lattice spots that were circled in Fig. 11c should be forbidden. Also, these spots could not be resulted by double diffraction. This meant that the U phase was not the η phase.

Furthermore, more ZAD patterns from the U phase grains were compared to simulated patterns from the most commonly seen intermetallic crystal structures that can be derived from the FCC structure, such as $L1_0$, $L1_2$ and $D0_{22}$; and none of these structures produced 100% match patterns to those obtained from U phase.

There was also speculation that the U phase might be a Ti-carbide [18,19] phase since this particular sample was oxidized in high CO_2 percentage atmosphere. Upon examining the U phase with TEM-EDS, no carbon could be found in the U phase grains, suggesting that this was not Ti-carbide. Moreover, the fact that twinning zone microstructure was present in an Inconel 939 sample oxidized in 1 atm of pure oxygen corroborated this conclusion.

It was therefore concluded that the U phase must have a new type of intermetallic crystal structure in either Ni–Ti or Ni–Ti–Ta systems, and it appeared to have a derivative crystal structure of FCC, because all of the FCC spots were present plus super-lattice spots positioned at half way of these fundamental

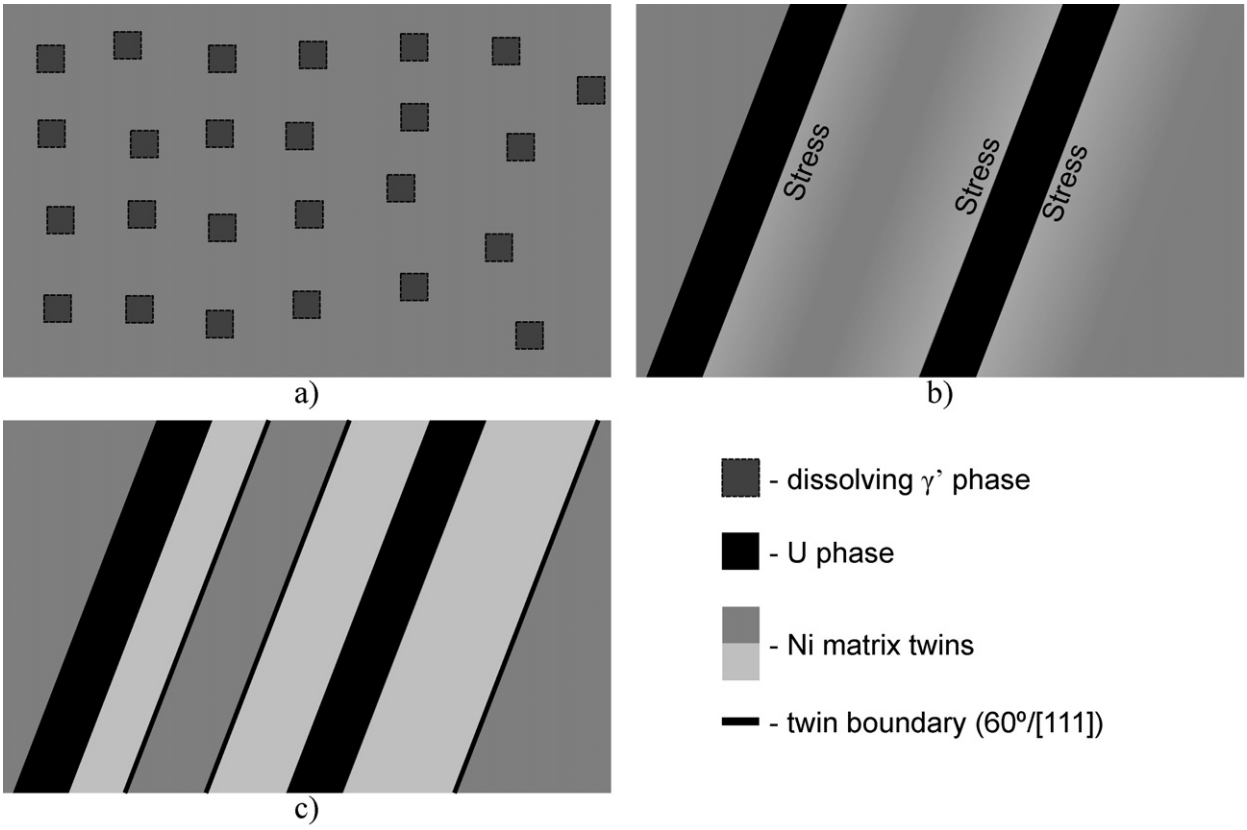

Fig. 10. Schematic drawing of the formation of the U phase and the twins.

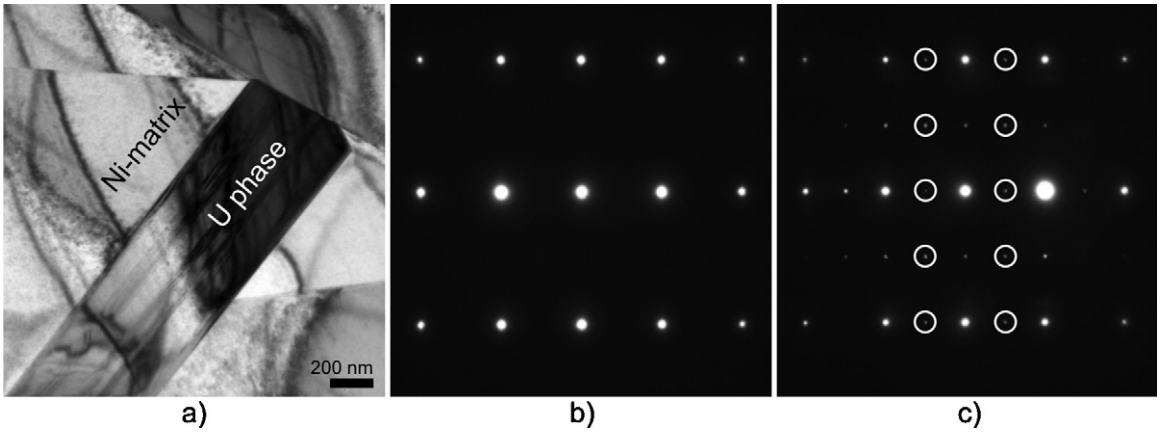

Fig. 11. (a) TEM bright field image of a Ni-matrix grain and a U phase grain. (b) The $[\bar{1}\,1\,\bar{2}]$ zone axis diffraction (ZAD) pattern of the Ni-matrix grain. (c) ZAD pattern from the U phase grain.

spots in reciprocal space. Further investigation is required to fully understand the crystal structure of the U phase.

3.4. The effect of U phase on oxidation and integrity of the alloy in service

3.4.1. Internal oxidation

The formation of the twinning zone and U phase can have mixed effects on the progression of internal oxidation. Since it was believed by the authors that twinning was a result of the local stress introduced by the formation of U phase, and that twin grain boundaries are generally more resistant to various types of corrosion than a random grain boundary (if grain boundary diffusion is involved in such corrosion) [20–23], the relatively large amount of twin grain boundaries in the Ni-matrix grain can to some extent restrict the progression of intergranular internal oxides. The downside effect from the U phase is that because Ti is enriched in the U phase grains, the U phase grains could become sources of more internal Ti-oxides and result in a mixture of internal oxides, which may render the sub-surface of the alloy prone to cracking or fatigue fracturing.

3.4.2. Mechanical integrity of the alloy

Due to the fact that U phase bears some resemblance to the TCP phase, especially that U phase contains a relative high content of refractory metal elements [13], it is reasonable to estimate that U phase would be brittle, compared to Ni-matrix grains, and thus detrimental. The elements that are effective in conferring creep resistance are depleted from the matrix and tied-up in the U phase, hence their solid solution strengthening effect is reduced. Also, the U phase may have similar detrimental effects as TCP precipitates such as de-lamination in the fracture zone [24], and void formation at high temperatures, which may potentially act as initiation sites for fracture [25,26].

4. Conclusions

(i) The oxidation microstructure for Inconel 939 Ni-based superalloy typically consisted of an external scale, an internal oxidation zone and an internal oxidation affected zone, which was characterized by a large amount of twinning.
(ii) The twinning zone microstructure could be the product of a phase transformation driven by a chemical composition change and assisted/restricted by local stress associated with the transformation. One of the two product phases, the U phase, was not in the Ni database of Thermo-Calc.
(iii) The phase constituents, FCC Ni-matrix and U phase in the twinning zone configured in a peculiar way, and this could be a result of relaxing the strain generated by the phase transformation.
(iv) The U phase has a new type of intermetallic crystal structure in either Ni–Ti or Ni–Ti–Ta systems, which are not well documented. Its crystal structure is a FCC derivative structure.
(v) The precipitation of U phase was believed to be detrimental to mechanical integrity of the alloy in use.

Acknowledgment

This technical effort was performed in support of the National Energy Technology Laboratory's ongoing research in advance combustion in gas turbine system under the RES contract DE-FE0004000.

References

[1] R.E. Anderson, S. Macadam, F. Viteri, D.O. Davies, J.P. Downs, A. Paliszewski, Proceeding of ASME Turbo Expo 2008: Power for Land, Sea and Air, Berlin, Germany (®2008 Clean energy systems Inc. and Siemens power generation Inc.) vol. 2, June, 2008, pp. 781–791.
[2] W. Sanz, H. Jericha, F. Luckel, E. Göttlich, F. Heitmeir, ASME Turbo Expo 2005: Power for Land, Sea and Air, ASME, Reno-Tahoe, Nevada, USA, 2005.
[3] R.E. Anderson, F. Viteri, R. Hollis, M. Hebbar, J. Downs, D. Davies, M. Harris, ASME Turbo Expo 2009: Power for Land, Sea and Air, ASME, Orlando, FL, 2009.
[4] H.J. Abel, U. Brill, T.I. Haubold, P. Klauke, Mater. Corros. 52 (2001) 283–288.
[5] F.A. Khalid, N. Hussain, K.A. Shahid, JMEPEG 6 (1997) 219–222.
[6] G.R. Holcomb, P. Wang, in: D. Gandy, J. Shingledecker, R. Viswanathan (Eds.), Proceedings of the 6th International Conference on Advances in Materials Technology for Fossil Power Plants, EPRI Report Number 1022300, ASM International, Materials Park, OH, 2011, pp. 312–324.
[7] Indranil Roy, PhD thesis, Precipitate growth features in the duplex size gamma prime distribution in the superalloy In738LC, Louisiana State University, 2003.
[8] W.J. Quadakkers, H. Schuster, Werkst. Korros. 36 (1985) 141–150.
[9] G. Sauthoff, Intermetallics, VCH, Weinheim, New York, 1995.
[10] D.J. Young, High Temperature Oxidation and Corrosion of Metals, Elsevier Ltd., Linacre House, Jordan Hill, UK, 2008.
[11] Thermo-Calc, Version S, Stockholm, Sweden: Thermo-Calc Software AB, 2008.
[12] N. Saunders, Ni-data, Version 8, Thermotech Ltd., Surrey Technology Centre, Guildford, Surrey GU2 5YG, U.K.
[13] J.X. Yang, Q. Zheng, X.F. Sun, H.R. Guan, Z.Q. Hu, Mater. Sci. Eng. A 465 (2007) 100–108.
[14] J.W. Morris Jr., A.G. Khachaturyan, S.H. Wen, in: H.I. Aaronson, D.E. Laughlin, R.F. Sekerka, C.M. Wayman (Eds.), Proceedings of the International Conference on Solid-Solid Phase Transformations, Pittsburgh, PA, 1981, pp. 101–126.
[15] K. Otsuka, K. Shimizu, in: H.I. Aaronson, D.E. Laughlin, R.F. Sekerka, C.M. Wayman (Eds.), Proceedings of the International Conference on Solid-Solid Phase Transformations, Pittsburgh, PA, 1981, pp. 1267–1286.
[16] P. Wollants, J.R. Roos, L. Delaey, Prog. Mater. Sci. 37 (1993) 227–288.
[17] A.J. Wilkinson, D.J. Dingley, G. Meaden, in: A.J. Schwartz, M. Kumar, B.L. Adams, D.P. Field (Eds.), Electron Backscatter Diffraction in Materials Science, Second edition, Springer Science+Business Media, LLC, 233 Spring Street, New York, 2009, pp. 231–249.
[18] P. Berthod, C. Vébert, L. Aranda, R. Podor, C. Rapin, Oxid. Met. 63 (2005) 57–72.

[19] J. Litz, A. Rahmel, M. Schorr, Oxid. Met. 30 (1988) 95–105.
[20] J. Zhu, L.M. Fernandez Diaz, G.R. Holcomb, P.D. Jablonski, C.J. Cowen, D.E. Laughlin, D. Alman, S. Sridhara, J. Electrochem. Soc. 157 (2010) B655–B664.
[21] L. Tan, K. Sridharan, T.R. Allen, R.K. Nanstad, D.A. McClintock, J. Nucl. Mater. 374 (2008) 270–280.
[22] V. Randle, The Role of the Coincidence Site Lattice in Grain Boundary Engineering, The Institute or Materials, London, 1996.
[23] V.B. Trindade, U. Krupp, Ph E.G. Wagenhuber, Y.M. Virkar, H.J. Christ, Mater. High Temp. 22 (2005) 207–212.
[24] M. Simonetti, P. Caron, Mater. Sci. Eng. A 254 (1998) 1–12.
[25] C.M.F. Rae, M.S.A. Karunaratne, C.J. Small, R.W. Broomfield, C.N. Jones, R.C. Reed, in: T.M. Pollock, R.D. Kissinger, R.R. Bowman, K.A. Green, M. McLean, M.L. Olson, J.J. Schirra (Eds.), Superalloys 2000, TMS, Warrendale, PA, 2000, p. 767.
[26] D.C. Cox, C.M.F. Rae, R.C. Reed, in: R. Townsend (Ed.), Life Assessment of Hot Section Gas Turbine Components, The Institute of Materials, London, UK, 2000, p. 119.